INSTITUTE OF PHYSICS PUBLISHING JOURNAL OF PHYSICS D: APPLIED PHYSICS

J. Phys. D: Appl. Phys. **34** (2001) 1933–1938 www.iop.org/Journals/jd PII: S0022-3727(01)20751-7

# Strobe imaging of electric fields by depolarization of Rydberg states of Hg

**Marcis Auzinsh, Lalith Jayasinghe, Lance Oelke, Ruvin Ferber and Neil Shafer-Ray**

The University of Oklahoma, Norman, OK 73019, USA

Received 11 January 2001, in final form 19 April 2001

**Abstract**

We present a new technique for imaging electric fields that takes advantage of the large field-dependent coupling of the Rydberg states of Hg. Specifically we demonstrate an optical scheme that takes advantage of the field-induced mixing of the $6s(^2\,S)nd\,D$ and $6s(^2\,S)(n+1)p\,P$ states of Hg. With the appropriate laser probe of this mixing, 579.2 nm light is produced that is directly related to the strength of the local electric field. This allows strobe images to be made of the electric field surrounding an object on a 50 ps timescale. We demonstrate the utility of this technique by probing the electric field surrounding pads on a digital integrated circuit package.

## 1. Introduction

The idea of taking advantage of the exaggerated Stark effect exhibited by Rydberg atoms to probe electromagnetic radiation dates to the work of Kleppner and Ducas [1]. The first use of Stark spectroscopy to image the spatial dependence of an electric field was carried out by Nakajima *et al* [2]. In 1989 Yang *et al* [3] demonstrated that the Stark effect could be used to achieve precise measurements of electric field strength. Since these early studies, many different field-dependent optical techniques have been implemented, primarily for the study of electric fields in glow discharge plasmas. These techniques have been reviewed by Lawler and Doughty [4]. Several notable advances have been made in the six years that have passed since this review was written. In 1994, the electric field in He discharge plasmas was measured directly by analysing the spatial dependence of the profile of the $1s11p^1\,P \rightleftharpoons 1s2s^1\,S$ transition [5]. This technique allowed for the measurement of the field without the introduction of a tracer gas. Another common element in discharge chemistry is atomic hydrogen; but to take advantage of the Stark effect in hydrogen, one must overcome the large Doppler widths typical of this light element. This has been accomplished using a double-resonance–double-free excitation scheme from the ground state to the $n = 6$ state [6]. A second innovation which improved sensitivity was fluorescence-dip spectroscopy of hydrogen atoms [7]. Here, the Stark spectrum of high-$n$ states of hydrogen atoms are probed by observing the reduction in Balmer-$\alpha$ radiation as $n = 3$ hydrogen is irradiated with a tunable source of IR radiation. It has also been suggested (but not demonstrated) that a broad-bandwidth laser could be used to probe electric fields in atomic hydrogen by taking advantage of the change in parity selection rules that occur in the presence of an electric field [8]. Finally, by analysing the splitting of the Balmer-$\alpha$ line of a beam of deuterium atoms in a tokamak plasma, it has become possible to gain sensitivity to the direction of the electric field [9].

Despite the large number of applications for which a spatial map of electric field strength might be useful, practical applications of probing electric fields using the Stark effect have been limited to fields in hostile environments such as plasmas, ovens at refractory temperatures, and rf discharges. Here we exploit the strong coupling of the $6s(^2\,S)(n+1)p\,P^o$ and $6s(^2\,S)(n-2)f\,F^o$ Rydberg series of Hg with the $6s(^2\,S)nd\,D$ series to create a qualitative map of electric fields in space. This strobe photographic technique, which we call Hg-Rydberg-state imaging (HgRSI), enables extended practical applications, including the testing of digital integrated circuits. To demonstrate the power of HgRSI, we have created a strobe image of the space above copper leads that connect the integrated circuit to the pins of a simple dip package. The images, shown in figure 1, are directly related to the field surrounding the chip in the 7 ns time interval during which our pulsed laser system strobes the field. Whereas the resolution of these photographs is limited by the time resolution of our sources of laser radiation, the theoretical limit is 50 ps, matching nicely the timescale of both current computer technology and commercial laser equipment. In its present form, the technique described is quantitative only if both the electric field direction and magnitude are constrained to a limited range. Despite this limitation, the probe scheme is sensitive to the difference between the field above a chip lead held at a potential of 5.0 V and the field above a grounded chip lead. This demonstrates that the technique may have

  

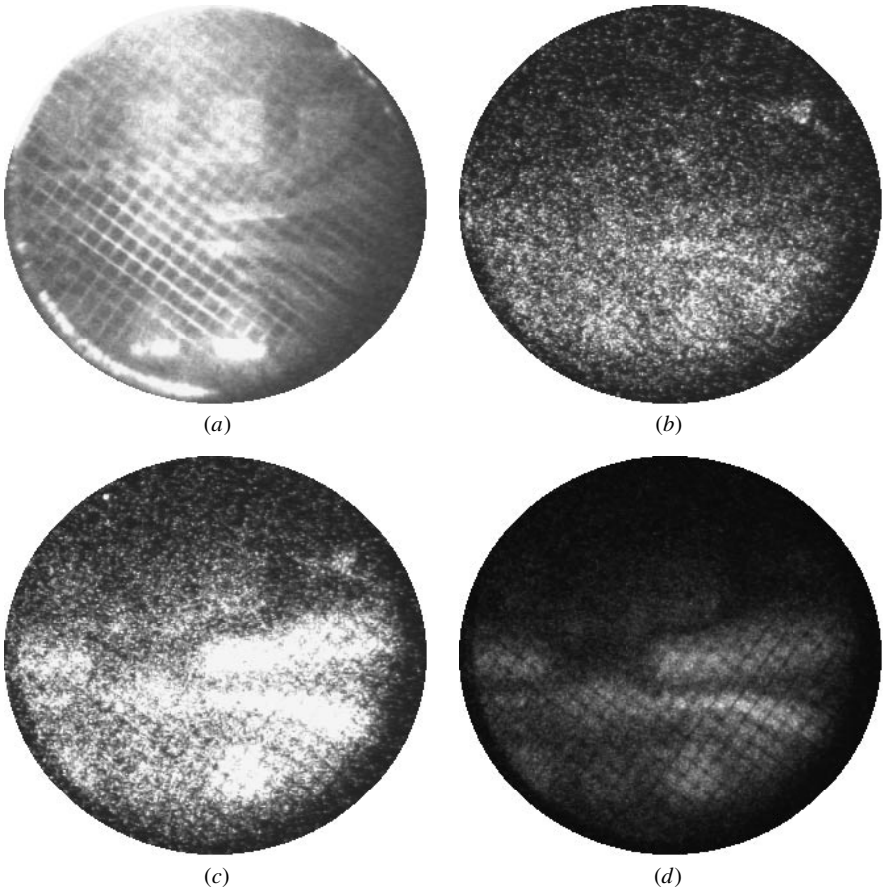


**Figure 1.** Image of pads on a standard 14 pin dip chip: (*a*) picture taken with ambient room light; (*b*) HgRSI image with all pads grounded; (*c*) HgRSI image with half of the pads at 5 V and the others grounded (pads at 5 V are illuminated by the probe laser radiation); (*d*) HgRSI image with half the pads at 10 V. Whereas the contrast of images (*b*) and (*c*) is identical, the contrast of image (*d*) is adjusted to accommodate a six-fold increase in fluorescence intensity.

applications as a high-speed, non-contact probe of digital signals.

In the next section we outline the spectroscopic scheme that makes this measurement possible. Section 3 presents a theoretical explanation of the sensitivity of this scheme to the electric field. Section 4 presents experimental tests of the scheme, including details of how the images shown in figure 1 have been created. We conclude with a list of specific advantages of HgRSI over previous field-imaging techniques.

## 2. Spectroscopic scheme

In the rest of the paper, we denote the $6s(^2\,S)(n+1)p\,P^o$, $6s(^2\,S)(n-2)f\,F^o$ and $6s(^2\,S)nd\,D$ Rydberg states by $(n+1)$p, $(n-2)$f and $n$d for brevity. Throughout this paper we have assumed we are exciting only the singlet transitions. However, the excited state spectra are complicated by the many isotopes of Hg and strong $j$–$j$ coupling. Thus it is entirely possible that the field-dependent spectra we observe are due to a combination of triplet and singlet Rydberg atoms. These highly excited Rydberg states consist of a tightly bound positively charged core and a single weakly bound Rydberg electron. The extreme sensitivity of such states to the electric field results from the fact that the electron has a non-vanishing probability of existing far away from the positive core. In this region the forces exerted by even relatively weak external fields are not negligible compared to the forces exerted by the core. Thus the wavefunction of the electron is easily distorted by external fields of moderate strength.

We first excite ground-state $6s^2\,^1S$ Hg to a member of the $n$d Rydberg series using two sources of laser radiation at 253.7 nm and about 226 nm. This scheme allows stepwise resonance enhancement from the $6s(^2\,S)6p^3\,P_1^o$ state (see figure 2). After the $n$d state is populated, an electric field rapidly distorts the wavefunction of the Rydberg electron. This distortion allows an otherwise parity-forbidden transition to the $6s(^2\,S)6d^1\,D_2$ state to be induced by ∼809 nm laser radiation. The extent to which the 809 nm laser radiation is able to populate the 6d state is related to the strength of the local electric field at the instant the lasers fire. The 6d state fluoresces 579.2 nm radiation as it decays to the 6p state. This fluorescence is easily separated from the 226, 253.7 and 809 nm light used to induce it. The fluorescence can be imaged to create a strobe photographic image of the electric field. (Alternatively, the 809 nm laser radiation could be tuned to the $n$d → 7p transition. This would result in field-dependent fluorescence at 140.2 nm as the 7p state decays to the ground state of Hg. This vacuum ultraviolet laser radiation could be detected directly using a microchannel plate detector. This scheme may have advantages for certain applications, but is not considered in the following sections.)

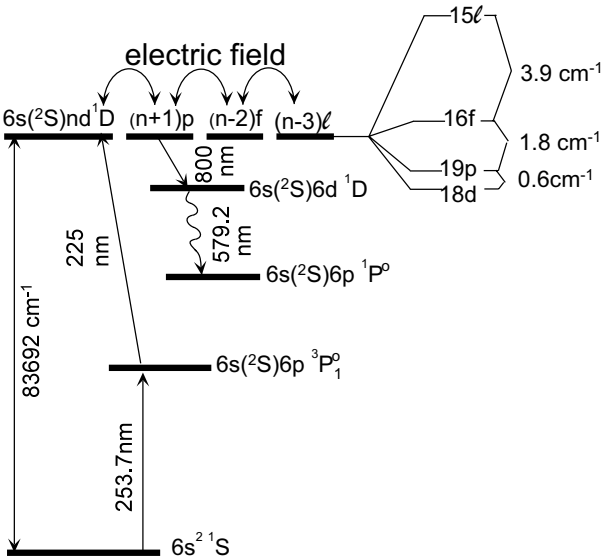


**Figure 2.** HgRSI scheme, as implemented in this work.

## 3. Theory of measurement

A quantitative theory of HgRSI requires us to consider the quantum theory of both Rydberg orbitals and the linear Stark effect. These theories are thoroughly reviewed in the comprehensive work of Gallagher on the topic [10]. This section presents the most important physics governing HgRSI, leaving the details to other sources.

Because the Rydberg electron wavefunction is large compared to the size of the core, it is accurately described by the quantum defect phase shifted Coulombic wavefunctions

$$|nlm\rangle = R_{n-\delta_l,l}(r)Y_{lm}(\theta,\phi). \tag{1}$$

Here $Y_{lm}(\theta,\phi)$ is the spherical harmonic and $R_{n-\delta_l,l}(r)$ is the solution to the radial equation that vanishes at infinity. The quantity $\delta_l$ is the quantum defect. For sufficiently high $n$, $\delta_l$ is a function of $l$ alone. For $\delta_l = 0$, $rR_{n-\delta_l,l}(r)$ vanishes at $r = 0$. In this case, $R_{n,l}(r)$ satisfies the radial boundary-value problem for a hydrogenic atom. For the Rydberg state of non-hydrogenic atomic system, $\delta_l$ is not zero because the atomic core modifies the boundary condition at $r = 0$. The new boundary condition not only modifies the radial wavefunction, but the energy of the orbital as well:

$$E_{n,l} = \frac{-R_\infty}{(n-\delta_l)^2}. \tag{2}$$

The quantum defects of the $(n+1)$p, $n$d and $(n-3)$f Rydberg series depend weakly on $n$. For $n = 18$, the defects of the p and d states, as determined from published tables [11], are $\delta_1 = 4.087$ and $\delta_2 = 3.096$. When pumping to the $n = 18$ state with laser radiation at 253.7 nm and 225.8 nm, we measure the HgRSI signal at dump wavelengths of 809.224 nm and 809.109 nm. We are confident that the final state for both of these dump transitions is the $6s(^2\,S)6d^1D$ state whereas we have tentatively assigned the initial states to correspond to the $19p^1\,P_1$ and $15p^1\,F_1$ levels. From this tentative assignment we conclude that there is a $1.75 \pm 0.05$ cm$^{-1}$ splitting between the $19p^1\,P_1$ and $15p^1\,F_1$ states and that $\delta_3 = 1.060$. The quantum defects of the Rydberg series for $\ell > 3$ are not measured, but should be very close to zero [10]. The fact that these defects differ by almost exactly an integer has the important consequence that the $(n+1)$p, $n$d, $(n-2)$f and $(n-3)(\ell > 3)$ series are very close in energy. The distortion of the $n$d wavefunction is due to mixing to these nearby angular momentum states.

To keep our analysis as straightforward as possible, we consider only the case in which all three sources of laser radiation are polarized along the same axis as the external electric field. If we choose our quantization axis along the electric field direction, this cylindrical symmetry causes $m$ to remains a good quantum number, both for the optical transitions and field mixing that occurs. Because the mercury begins in a $^1$S state, we need only consider states for which $m = 0$. We further assume that, at $t = 0$, the initial state (as populated by the 253.7 and 226 nm *laser radiation*) is given by the pure state

$$\psi(t=0) = |n, 2, 0\rangle\,. \tag{3}$$

Under the assumption that only the nearly degenerate $(n+1)$p, $n$d, $(n-2)$f and $(n-3)(\ell > 3)$ states contribute to the evolution of the Rydberg electron, the time-dependent wavefunction will be given by

$$\psi(t) = c_1(t)\,|n+1, 1, 0\rangle + c_2(t)\,|n, 2, 0\rangle + c_3(t)\,|n-2, 3, 0\rangle + \sum_{l=4}^{n-3} c_l(t)\,|n-3, l, 0\rangle \tag{4}$$

where the evolution of the coefficients is determined from Schrödinger's equation to be

$$\mathrm{i}\frac{\partial \vec{c}}{\partial t} = \left[A^{\mathrm{E}} + FA^{\mathrm{M}}\right]\vec{c}. \tag{5}$$

Here $A^{\mathrm{E}}_{ij}$ and $A^{\mathrm{M}}_{ij}$ are $(n-3)\times(n-3)$ matrices and $F$ is the strength of the electric field. The matrix $A^{\mathrm{E}}$ is a diagonal matrix defined by the energy levels of each of the states:

$$A^{\mathrm{E}}_{\ell\ell'} = \begin{cases} -R_\infty\delta_{\ell\ell'}\left[\frac{\delta_{\ell,1}}{(n+1-\delta_1)^2} + \frac{\delta_{\ell,2}}{(n-\delta_2)^2} + \frac{\delta_{\ell,3}}{(n-2-\delta_3)^2} - \frac{1}{(n-3)^2}\right] & \ell \leqslant 3 \\ 0 \quad \text{for} & \ell > 3. \end{cases} \tag{6}$$

We have chosen the zero energy to correspond to the energy level of the high-angular momentum states so that only three terms in this diagonal matrix are nonzero.

The mixing matrix $A^{\mathrm{M}}$ is defined by the dipole moments

$$A^{\mathrm{M}}_{\ell\ell'} = \langle n'\ell'm'|ez|n\ell m\rangle \tag{7}$$

with $m = m' = 0$. For the case that $n' = n$ and $\delta_l = \delta_{l'} = 0$, the mixing elements can be shown [12] to be given by

$$\langle n\ell'm'|ez|n\ell m\rangle = \frac{3ea_0}{2}(-1)^m\delta_{m,m'}\delta_{|\ell-\ell'|,1}n \times\sqrt{\frac{\left(l_x^2-m^2\right)\left(n^2-l_x^2\right)}{4l_x^2-1}}. \tag{8}$$

Here $e$ is the electronic charge, $a_0$ is the first Bohr radius, $l_x = \max(\ell,\ell')$, and $\delta_{m,m'}$ and $\delta_{|\ell-\ell'|,1}$ are Kronecker delta functions. For the studies here, we are only interested in nearly

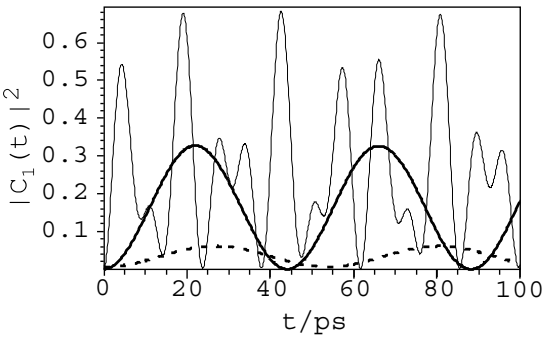


**Figure 3.** Time-dependent population $|c_1(t)|^2$ of the $19p^1\,P^o$ state after excitation to the $18d^1$ D state in the presence of electric fields of strengths 10 V cm$^{-1}$ (dashed line), 30 V cm$^{-1}$ (solid heavy line) and 200 V cm$^{-1}$ (solid light line).

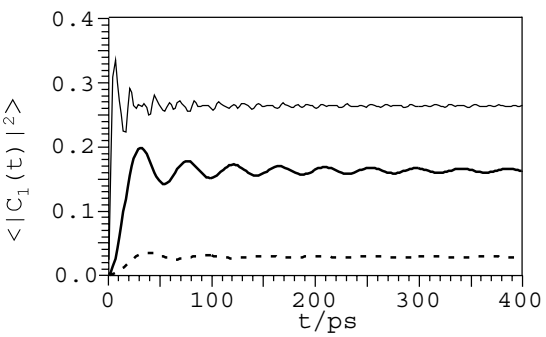


**Figure 4.** Time-averaged population $\frac{1}{t}\int_0^t |c_1(t')|^2 dt'$ of the $19p^1\,P^o$ state after excitation to the $18d^1$D state in the presence of electric fields of strengths 10 V cm$^{-1}$ (dashed line), 30 V cm$^{-1}$ (solid heavy line) and 200 V cm$^{-1}$ (solid light line).

degenerate states with $n-\delta_l \approx n'-\delta'_l$. Except for regions very close the core, the Coulombic radial wavefunctions vary smoothly as a function $n-\delta_l$ and $n'-\delta'_l$. We therefore expect the exact form of (8) to remain valid with the substitution of $n-\delta_l$ for $n$. Indeed this intuitive picture is supported by the more rigorous work of Picart *et al* [13], that leads to

$$\left\langle n'\ell'm'|e\,z|n\ell m\right\rangle = \frac{3ea_0}{2}(-1)^m\delta_{m,m'}\delta_{|\ell-\ell'|,1}\nu_c \times\sqrt{\frac{\left(l_x^2-m^2\right)\left(\nu_c^2-l_x^2\right)}{4l_x^2-1}}\phi \tag{9}$$

where

$$\nu_c = \frac{2(n-\delta_l)(n'-\delta_{l'})}{(n-\delta_l)+(n'-\delta_{l'})} \tag{10}$$

$$\approx n-\delta_l. \tag{11}$$

Here $\phi$ is the ratio of this approximate form to the exact matrix element. This parameter can easily be determined using the work of Edmunds *et al* [14]. For the 18d $\rightleftharpoons$ 19p mixing considered here, the matrix element obtained by substituting $n-\delta_l$ for $\nu_c$ and 1 for $\phi_c$ is within 0.4% of the exact value whereas the approximate 18d $\rightleftharpoons$ 19f matrix element is in error by 0.6%. These corrections do not affect the agreement of our experiment with the theory presented here.

The probability of excitation of the $6d^1$ D state by the 809 nm dump laser radiation is proportional to the population

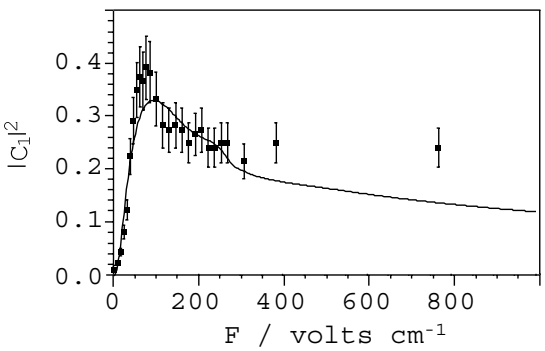


**Figure 5.** Time-averaged population $|c_1|^2 = \lim_{t\to\infty}\frac{1}{t}\int_0^t |c_1(t')|^2\,dt'$ of the $19p^1\,P^o$ state after excitation to the $18d^1$ D state as a function of an applied field. The solid line is taken from the solution to equation (5) of the text whereas the points give the experimentally obtained field dependence of the 579.2 nm fluorescence of the HgRSI scheme.

of the $(n+1)p^1\,P^o$ state, which is in turn proportional to $|c_1(t)|^2$. Figure 3 shows $|c_1(t)|^2$ for Hg initially excited to the $18d^1$ D state in the presence of 10, 30 and 200 V cm$^{-1}$ fields. For each case, the population $|c_1(t)|^2$ varies on a picosecond timescale. Figure 4 gives the time-averaged value of $|c_1(t)|^2$ as a function of the period of the time integral. For 10, 30 and 200 V cm$^{-1}$ fields, the time-averaged values of $|c_1(t)|^2$ fluctuate by less than 10% of the asymptotic values after 50 ps. Thus, provided the strobe laser radiation occurs for more than 50 ps (as is the case of our 7 ns pulsed laser system) the HgRSI probe is sensitive primarily to the time-averaged population of the $(n+1)$p state. Figure 5 gives this time-averaged population as a function of field strength for the case $n = 18$. This population is compared to experiment in the next section.

Even in the limit of a weak field, the response of the HgRSI probe is very fast. In this limit, only mixing between the 18d and 19p states is significant. This results in a two-level problem that can be solved analytically. Its solution shows that $|c_1(t)|^2$ oscillates sinusoidally. In the limit of zero field, the frequency of this oscillation does not go to zero, but rather to $\Delta E/h = 56$ ps, where $\Delta E$ is the splitting between the 18d and 19p states.

## 4. Experimental details

A 7 ns Nd:YAG laser (Continuum Shurlite IIe) is used to pump a dye laser (Spectra Physics PDL II, exciton C500 dye) with 355 nm laser radiation. The output of this dye laser is doubled using a BBO crystal to create 253.7 nm radiation. This UV radiation is used to excite ground-state Hg to the $6p^3\,P_1^o$ state. To reduce background due to scattered 253.7 nm fluorescence, a 25–40 ns time delay is added between the creation of the $6p^3\,P_1^o$ state and excitation to the $n$d state. Because the lifetime of the $6p^3\,P_1^o$ state is much greater than 40 ns, this time delay does not significantly affect the sensitivity of the probe.

The laser radiation responsible for both excitation to the $n$d state and the subsequent induced emission to the 6d state is created by a second 7 ns Nd:YAG pumped dye laser system (Nd:YAG laser by Larry Wolford Systems). Approximately 80% of the 532 nm output of this Nd:YAG laser pumps a dye laser to produce ∼675 nm radiation that is frequency tripled

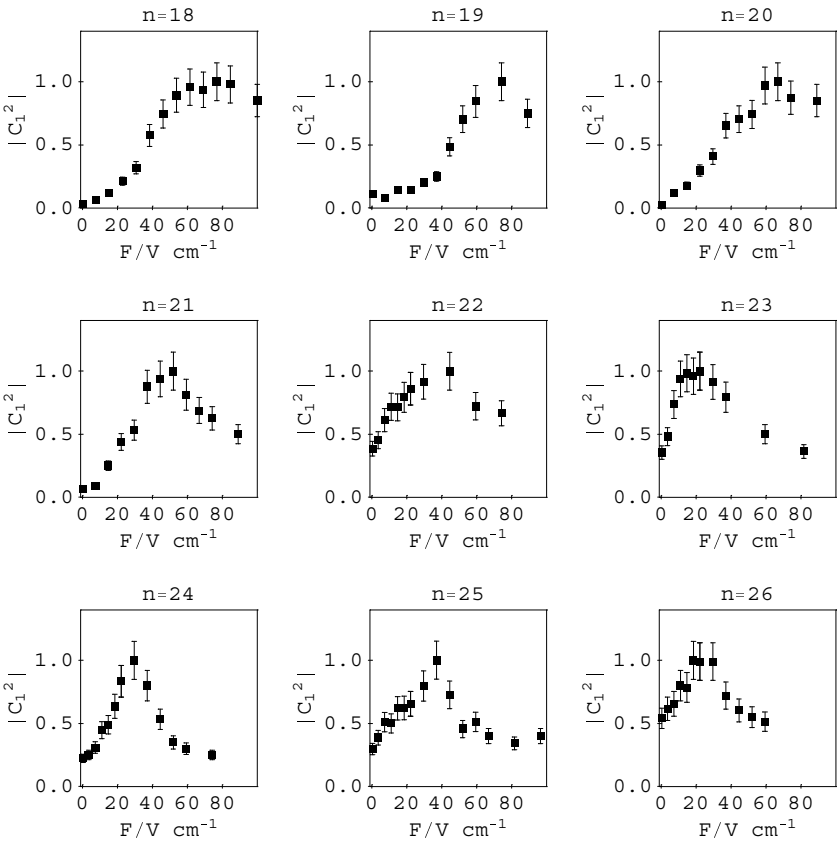


**Figure 6.** Experimentally obtained 579.2 nm fluorescent yield of the HgRSI scheme as a function of $n$ and field strength.

using KDP and BBO crystals. The resulting ∼226 nm radiation is used to excite Hg from the $6p^3\,P_1^o$ state to the $nd^1$ D state. The remaining 20% of the 532 nm output of the Nd:YAG laser pumps a second dye laser to produce ∼809 nm radiation that is used to induce Hg to change from the $n$d state to the $6d^1$ D state. Whereas the pulse width of the laser system used to create the 253.7 nm fluorescence does not greatly influence the measurement, the 7 ns pulse width of the second Nd:YAG laser limits the response time of the strobe. For excitation to the 18d state, this Nd:YAG laser system should be replaced with a picosecond pulsed laser system to minimize the strobe time.

To test the sensitivity of HgRSI to the electric field, the three probe lasers are focused into the centre of two parallel square conducting plates placed in the centre of a vacuum chamber. The sides of the plates are of 8 cm dimension and the plates are separated by 1.3 cm. The polarization of all three sources of laser radiation is normal to the plane of the plates. A 3 cm diameter hole is placed in the top plate and covered with a stainless-steel mesh. An interference filter and a photomultiplier tube are used to measure the yield of induced 579.2 nm fluorescence from the 6d state as a function of the voltage difference between the plates. Figure 5 illustrates that for $n = 18$, the experimentally obtained field dependence is in reasonable agreement with the theory of the previous section provided the field strength is below 400 V cm$^{-1}$. The only adjustable parameter in this comparison is a single scale factor used to normalize the experimental data. The disagreement between theory and experiment at high field strengths is caused by either mixing of singlet and triplet states or by the inaccuracy of our assumption that states with $\ell > 3$ have a zero quantum defect. Also the triplet Rydberg states may be contributing to the HgRSI fluorescence.

For $n > 18$, the splittings between the $(n+1)$p, $n$d, $(n-2)$f and $(n-3)\ell$ states are not known with sufficient accuracy to make quantitative predictions. Figure 6 gives experimental curves for $n = 18$–26. For $n > 21$, the fluorescence we observe is no longer close to zero at zero field. The zero-field signal is observed to have a strong dependence on background pressure, indicating that it is caused by collisional mixing of the excited Rydberg states.

To create the electric field image of figure 1, a trinocular microscope is used to image the leads of the carrying signal from the pins of a standard dip package to the integrated circuit (figure 7). The dip package is prepared by sanding off the plastic insulating material covering a 74LS04 inverting gate. The integrated circuit is destroyed in this process, allowing us to bias each pin to a continuous range of voltages. A uniform mesh is placed approximately 3 mm above the chip. An image-intensified CCD array (Roper Scientific ICCD camera) is mounted behind a trinocular microscope and 580 nm interference filter. Ambient room light is used to create a picture of the sample (figure 1($a$)). The three probe laser sources were then focused cylindrically a distance of 0.3 mm over the top of the integrated circuit. As the lasers fire at a repetition rate of 10 Hz, the gated CCD camera collects the 579.2 nm fluorescence.

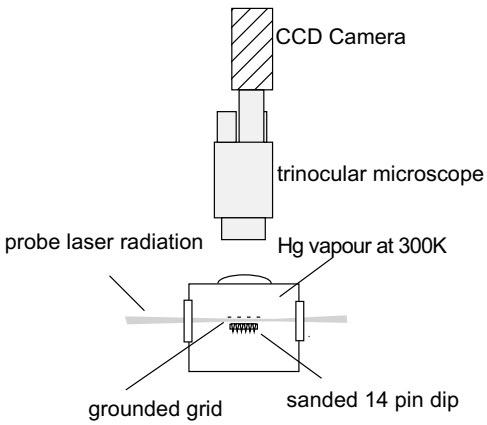


**Figure 7.** Schematic diagram of the experimental set-up used to create the images shown in figure 1.

## 5. Summary of the HgRSI technique

The HgRSI technique described here is a high-speed and sensitive laser-induced fluorescence probe of electric field strength. This probe scheme produces fluorescence intensity that grows monotonically from no fluorescence to maximum fluorescence as the electric field increases from 0 to $\sim$60 V cm$^{-1}$. For fields greater than $\sim$60 V cm$^{-1}$, the fluorescence intensity drops off slowly. More development is needed to use this technique for precise field measurements over a large dynamical range. However, for applications for which both the magnitude and direction of the electric field are constrained to a narrow range, the technique may already be useful. A possible application is the simultaneous determination of the digital state of a large number of test points on an electronic circuit board running at frequencies up to 100 GHz.

HgRSI solves many of the problems that have kept Stark imaging from being applied to many test environments. Here we conclude with a list of the important advantages of this technique.

(1) To use any Stark imaging technique, the trace gas must be uniformly distributed about the spatial region of interest. A uniform distribution is difficult to obtain if the temperature required to introduce the trace gas is greater than the maximum temperature that can be sustained by the object one wishes to study. A uniform distribution is equally difficult to sustain if a radical species (such as hydrogen) is required. The vapour pressure of Hg at room temperature [15] is 2.0 mTorr. This ideal vapour pressure not only makes it straightforward to obtain a uniform distribution of Hg in the probe region, but makes it trivial to introduce the gas into the system being studied.

(2) In many studies, one must probe a relatively large object such as a computer chip. This requires the strobe laser to be spread over a large area, limiting the intensity of the radiation. HgRSI is feasible in these cases because strong sources of pulsed laser radiation at the required wavelengths are obtainable with conventional laser technology. Furthermore, each source of radiation drives a strong single-photon atomic transition.

(3) The HgRSI probe presented here has a $\sim$50 ps response time. Thus HgRSI is nimble enough to keep up with the nanosecond timescale of the modern digital electronics industry.

(4) The samples one may wish to probe are not designed to minimize scattered light as would be the case in a laboratory environment. Thus background from scattered fluorescence of the strobe laser radiation is of great concern. For the HgRSI technique, ultraviolet and infrared wavelengths are used to strobe the electric field whereas visible or vacuum ultraviolet fluorescence may be used to detect its presence. Thus the induced fluorescence is easily isolated from the strobe radiation, and the effect of scattered light is minimized.

(5) This technique relies on dipole selection rules rather than on-line profile analysis to gain sensitivity to electric field strength. This allows broad-bandwidth strobe laser radiation to be used. This feature is critical if short pulses of laser radiation are to be used.

(6) When probing complex systems, one may not know before a measurement is made what the range of electric field strength will be. The choice of the excited Rydberg state creates control over the sensitivity range, and hence the contrast of the image created.

## Acknowledgments

This work has benefited from money from the University of Oklahoma's office for the Vice President of Research, The National Science Foundation (CHE-9875456), and the National Research Council (NRC-6224.) We also acknowledge useful input from Gregory Parker and Michael A Morrison.

## References

[1] Kleppner D and Ducas T W 1976 *Bull. Am. Phys. Soc.* **21** 600
[2] Nakajima T, Uchitomi N, Adachi Y, Maeda S and Hirose C 1983 *J. Phys. Colloq.* C **7** 497
[3] Yang D, Lieberman D and van der Straten P 1989 *Phys. Rev.* A **40** 5026
[4] Lawler J E and Doughty D A 1994 *Adv. At. Mol. Opt. Phys.* **34** 171
[5] Hebner G, Greenberg K and Riley M 1994 *J. Appl. Phys.* **76** 4036
[6] Booth J P, Fadlallah M J D and Sadeghi N 1994 *Appl. Phys. Lett.* **65** 819
[7] Czarnetzki U, Luggenholscher D and Dobele H F 1998 *Phys. Rev. Lett.* **81** 4592
[8] Shafer-Ray N E and Zare R N 1996 *Appl. Phys. Lett.* **69** 3749
[9] Rice B W, Burrell K H, Lao L L and Lin-Liu Y R 1997 *Phys. Rev. Lett.* **79** 2694
[10] Gallagher T 1994 *Rydberg Atoms (Cambridge monographs on atomic, molecular and chemical physics)* (New York: Cambridge University Press)
[11] Moore C E 1971 *National Bureau of Standards Reference Data* 192
[12] Bethe H A and Salpeter E E 1977 *Quantum Mechanics of One- and Two-Electron Atoms* (New York: Plenum)
[13] Picart J, Edmonds A R and Minh N T 1978 *J. Phys. B: At. Mol. Phys.* **11** L651
[14] Edmonds A R, Picart J, Minh N T and Pullen R 1979 *J. Phys. B: At. Mol. Phys.* **12** 2781
[15] Alcock C, Itkin V and Horrigan M 1984 *Can. Metall. Q.* **23** 309